catalysts

MDPI

Article

TiO_2-Based Heterostructure Containing *g*-C_3N_4 for an Effective Photocatalytic Treatment of a Textile Dye

Martina Kocijan [1,*], Milan Vukšić [1,*], Mario Kurtjak [2], Lidija Ćurković [1,*], Damjan Vengust [2] and Matejka Podlogar [3,*]

[1] Department of Materials, Faculty of Mechanical Engineering and Naval Architecture, University of Zagreb, Ivana Lučića 5, 10000 Zagreb, Croatia
[2] Advanced Materials Department, Jožef Stefan Institute, Jamova cesta 39, SI-1000 Ljubljana, Slovenia
[3] Department for Nanostructured Materials, Jožef Stefan Institute, Jamova cesta 39, SI-1000 Ljubljana, Slovenia
* Correspondence: martina.kocijan@fsb.hr (M.K.); milan.vuksic@fsb.hr (M.V.); lidija.curkovic@fsb.hr (L.Ć.); mateja.podlogar@ijs.si (M.P.)

Abstract: Water pollution has become a serious environmental issue. The textile industries using textile dyes are considered to be one of the most polluting of all industrial sectors. The application of solar-light semiconductor catalysts in wastewater treatment, among which TiO_2 can be considered a prospective candidate, is limited by rapid recombination of photogenerated charge carriers. To address these limitations, TiO_2 was tailored with graphitic carbon nitride (*g*-C_3N_4) to develop a heterostructure of *g*-C_3N_4@TiO_2. Herein, a simple hydrothermal synthesis of TiO_2@*g*-C_3N_4 is presented, using titanium isopropoxide (TTIP) and urea as precursors. The morphological and optical properties and the structure of *g*-C_3N_4, TiO_2, and the prepared heterostructure TiO_2@*g*-C_3N_4 (with different wt.% up to 32%), were analyzed by various laboratory methods. The photocatalytic activity was studied through the degradation of methylene blue (MB) aqueous solution under UV-A and simulated solar irradiation. The results showed that the amount of *g*-C_3N_4 and the irradiation source are the most important influences on the efficiency of MB removal by *g*-C_3N_4@TiO_2. Photocatalytic degradation of MB was also examined in realistic conditions, such as natural sunlight and different aqueous environments. The synthesized *g*-C_3N_4@TiO_2 nanocomposite showed superior photocatalytic properties in comparison with pure TiO_2 and *g*-C_3N_4, and is thus a promising new photocatalyst for real-life implementation. The degradation mechanism was investigated using scavengers for electrons, photogenerated holes, and hydroxyl radicals to find the responsible species for MB degradation.

Keywords: UV-A; simulated solar light; natural sunlight; *g*-C_3N_4@TiO_2; water matrices; scavengers

Citation: Kocijan, M.; Vukšić, M.; Kurtjak, M.; Ćurković, L.; Vengust, D.; Podlogar, M. TiO_2-Based Heterostructure Containing *g*-C_3N_4 for an Effective Photocatalytic Treatment of a Textile Dye. *Catalysts* **2022**, *12*, 1554. https://doi.org/10.3390/catal12121554

Academic Editors: Huan Li and Jiabai Cai

Received: 20 October 2022
Accepted: 28 November 2022
Published: 1 December 2022

1. Introduction

Wastewaters contain harmful chemicals and different elements that have been released into rivers, lakes, and seas, consequently damaging the marine life and harming human health as well. Wastewater treatment plants are a standardized way to mitigate the harmful effect of industrial wastewater and preserve the environment. Considering the types of waste and the amount of waste generated, industrial wastewater treatment plants face the challenge of processing substantial amounts of waste using conventional technology [1]. Innovative technologies, such as advanced oxidation processes (AOPs), UV irradiation, and membrane filtration, show great promise in tackling this issue [2,3]. AOPs are based on highly reactive radicals, especially the hydroxyl (•OH) radical, due to their capability to significantly accelerate the pollutant oxidation. The generation of •OH radicals is commonly triggered by hydrogen peroxide (H_2O_2), titanium dioxide (TiO_2), and heterogeneous photocatalytic processes [4]. The latter hold the greatest promise for water and wastewater detoxification due to mild operating conditions and utilization of photon energy, which can be introduced as carbon-neutral renewable solar energy. In addition, heterogeneous

photocatalysis with absorption of the incoming photons in a semi-conductor material is expected to have advantages in industrial practice, such as simpler re-use and separation from the liquid medium, supported by cheaper and more durable catalysts [5–7].

The most common semiconductor in heterogeneous photocatalysis is titanium dioxide (TiO_2) due to its stability, high photocatalytic productivity, satisfactory band-edge potential [8–10]. To further improve photosensitizing potential, hybrid or composite materials are developed on the laboratory scale. Utilizing solar light energy harvesting, i.e., moving from UV to visible light by narrowing the band gap, is especially crucial for practical use [11].

To date, different single-metal oxides have been coupled with *g*-C_3N_4 to enhance the visible-light photocatalysis, especially TiO_2 (band gap around 3.2 eV) [12,13]. Additionally, TiO_2 has a suitable band edge position for combination with *g*-C_3N_4 (band gap between 2.4 and 2.8 eV) to improve its photocatalytic activity [14]. Miranda et al. [15] reported that the photocatalytic efficiency of a TiO_2 composite with 2 wt.% *g*-C_3N_4 in phenol degradation was higher by 35% compared to pure TiO_2. The study of Boonprakob et al. [16] demonstrated an improved photocatalytic activity and better generation of active species because of heterojunction formation and band gap narrowing.

Methylene Blue (MB) and Rhodamine B (RhB) are frequently used as model pollutants because of their high stability in aqueous media at ambient conditions [17,18]. The composite *g*-C_3N_4@TiO_2 heterojunction showed the capability to degrade these pollutants [19–21]. Razali et al. [22] observed the improved photocatalytic activities under visible light over the prepared g-C_3N_4/TiO_2, using a simple hydrothermal method and $TiCl_4$ as a precursor, where the prepared sample exhibited high photocatalytic activity in the degradation of MB".

The conducted studies on degradation of RhB detected higher impact of $O_2^{\bullet -}$, while a lower impact of holes (h^+) was noticed [23,24]. Considering MB degradation, the findings by Razali et al. [22] suggested a significant impact of both reactive oxygen species. Li et al. [25] achieved a significant improvement of MB degradation under visible light by Ti^{3+} self-doped TiO_2 nanoparticles/*g*-C_3N_4 heterojunctions. A recent study demonstrated the feasibility of the practical implementation of *g*-C_3N_4@TiO_2 composite in the degradation of dye pollutants (MB and RhB) by using parabolic trough collectors as a continuous flow loop photoreactor [26].

Overall, studies described above reported the improved photocatalytic activities under UV and visible light over g-C_3N_4/TiO_2 photocatalysts, suggesting the potential application of them in environmental remediation. This study differs from similar studies by applying a facile and cost-effective hydrothermal method with a lower temperature of 300 °C for preparation of catalysts. and by the investigation of photocatalytic activity in various aquatic matrices. More precisely, our goal was to develop TiO_2-based heterostructure containing *g*-C_3N_4 by a simple hydrothermal synthesis. This method was chosen due to its environmental friendliness; the possibility of controlling the size distribution, shape, and chemical composition of synthesized materials; and an easy scale-up for industrial use [27]. The photocatalytic activity was investigated by photodegradation of an aqueous solution of MB under UV-A, simulated solar, and natural sunlight. The novelty of the conducted study was to investigate the prepared *g*-C_3N_4@TiO_2 nanocomposite under realistic conditions, such as natural sunlight sources, irradiation, and environmental water. Such investigation is of utmost importance to reduce the research gap between theoretical knowledge and practical implementation for wastewater treatment.

2. Results and Discussion

2.1. Characterization of the Prepared Materials

The crystalline phase structures of the prepared materials were characterised by X-ray diffraction. Figure 1 shows the XRD patterns for *g*-C_3N_4, TiO_2, and *g*-C_3N_4@TiO_2 with various wt.% of *g*-C_3N_4. The prepared pure *g*-C_3N_4 exhibits two characteristic maxima at 13.04° and 27.36°, corresponding to (100) and (002) crystal planes, respectively. They could be attributed to the in-plane ordering of the tri-*s*-triazine units and the interplanar stacking

of conjugated aromatic units, respectively [28–30]. Additionally, the diffraction pattern matches well with the hexagonal JCPDS 01-087-1526 C_3N_4 standard from the database. Although some deviation has been noticed, probably related to calcination temperature. Namely, the (002) maximum appeared at 27.36° rather than at 26.51° [31]. The pure TiO_2 XRD pattern corresponds to a predominantly anatase-type phase in TiO_2 (JCPDS 21-1272) with maxima at 2θ values of 25.33°, 37.67°, 47.97°, 54.04°, 55.03°, 62.69°, 68.86°, 70.21°, 75.06°, 82.85°, corresponding to (101), (004), (200), (105), (211), (204), (116), (220), (215) crystal planes, respectively, and remains unchanged upon addition of *g*-C_3N_4 into the composites. Only a very low *g*-C_3N_4 (002) maximum can be distinguished in the XRD pattern of *g*-C_3N_4@TiO_2, with the highest (32 wt.%) *g*-C_3N_4 amount slightly overlapping with the (101) maximum of TiO_2 anatase phase.

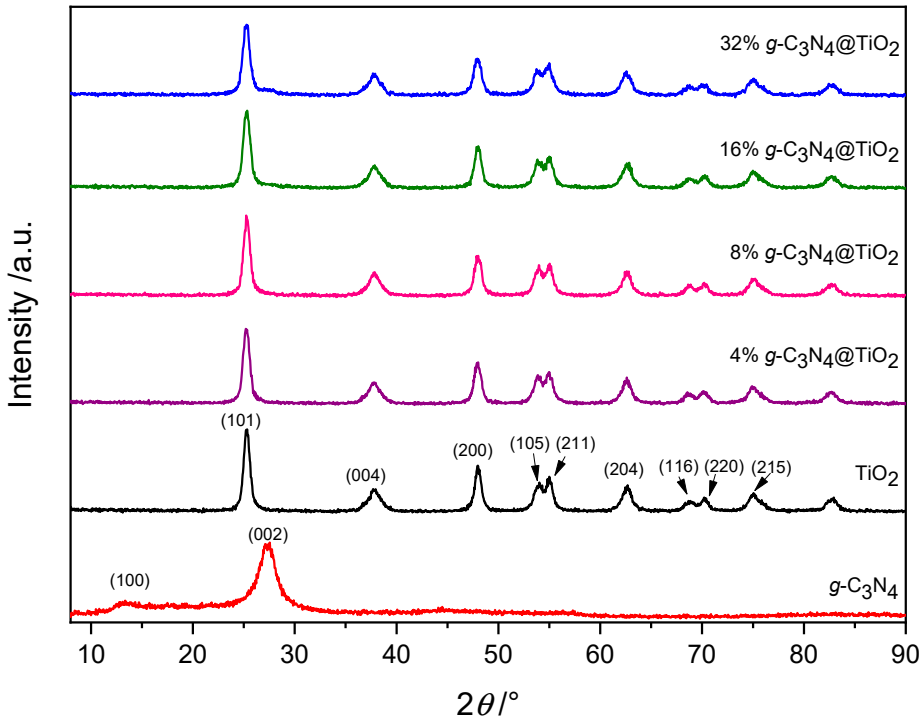

Figure 1. XRD patterns of prepared materials.

The results of FTIR analysis are shown in Figure 2, which was carried out to further confirm the composition of the *g*-C_3N_4@TiO_2 nanocomposites. Figure 2A shows the FTIR spectra of pure *g*-C_3N_4, TiO_2, and *g*-C_3N_4@TiO_2 nanocomposites. It shows that *g*-C_3N_4@TiO_2 nanocomposites match all major peaks of *g*-C_3N_4 and TiO_2 (shown in Figure 2B), by which their presence in the composites is additionally confirmed. Pure TiO_2 demonstrates bands in the region of 400–700 cm^{-1} due to Ti–O–Ti stretching vibration, while O–H stretching vibration occurs around 3400 cm^{-1} [32]. The heat treatment at 300 °C resulted in the decomposition of organic surfactants, which is indicated by the lack of any vibrational modes of Ti–OH and C–H in the IR spectra of TiO_2 (Figure 3), suggesting the destruction of hydroxy groups [33]. Pure *g*-C_3N_4 demonstrates strong bands in regions of 1200–1700 cm^{-1} which confirms that *g*-C_3N_4 was prepared successfully. The obtained results are consistent with the XRD results. The stretching vibration of C-N is represented at 1629.2 cm^{-1}. Bands at 1531.9, 1457.5, and 1394.6 cm^{-1}, are related to the aromatic C=N bond vibrations, while the peaks located at 1311.6 and 1228.7 cm^{-1} correspond to the stretching vibration of C-NH bond [34]. Absorption in the 2900–3600 cm^{-1} region led to NH group stretching modes. Finally, the noticeable peak at 820 cm^{-1} could be attributed to characteristic modes of the heptazine ring structure [35,36]. With different loading concentration of *g*-C_3N_4 into TiO_2, the structural changes of *g*-C_3N_4 can be observed. Most noticeably, the weakening of the peak at 820 cm^{-1} corresponding to symmetric vibration

of the C-N heterocycle indicates that the symmetry of the ring is lost in the heterostructures due to possible bonding with TiO_2. Relative values of the peaks corresponding to individual carbon nitride vibrations are also altered. Another significant change can be observed with the N-H vibrations on the surface of the g-C_3N_4, which were suspended especially at lower concentrations, suggesting chemical bonding of the two components within the composite.

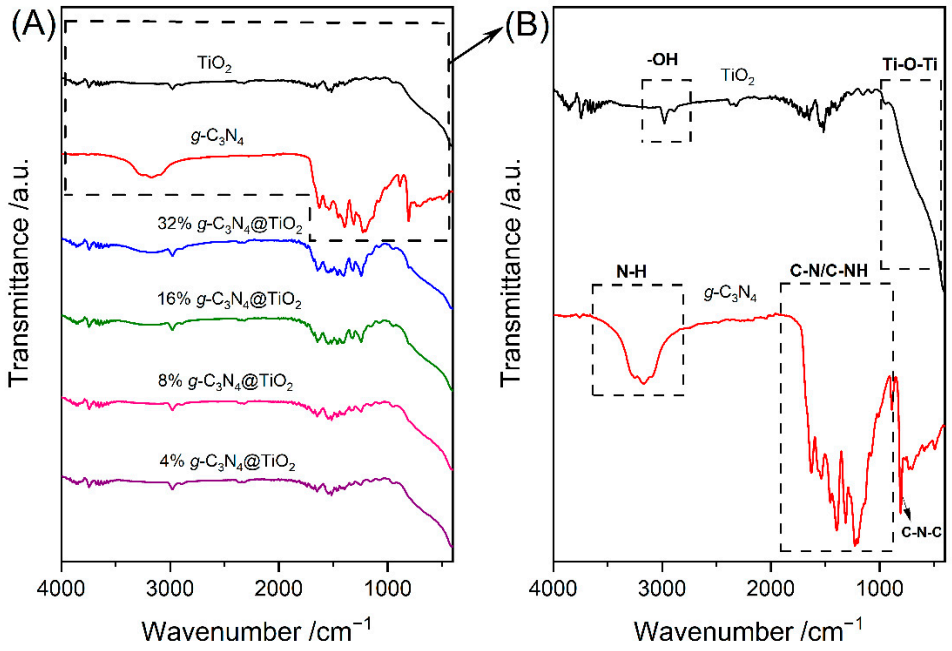

Figure 2. (**A**) FTIR spectra of the representative samples and (**B**) pure TiO_2 and g-C_3N_4.

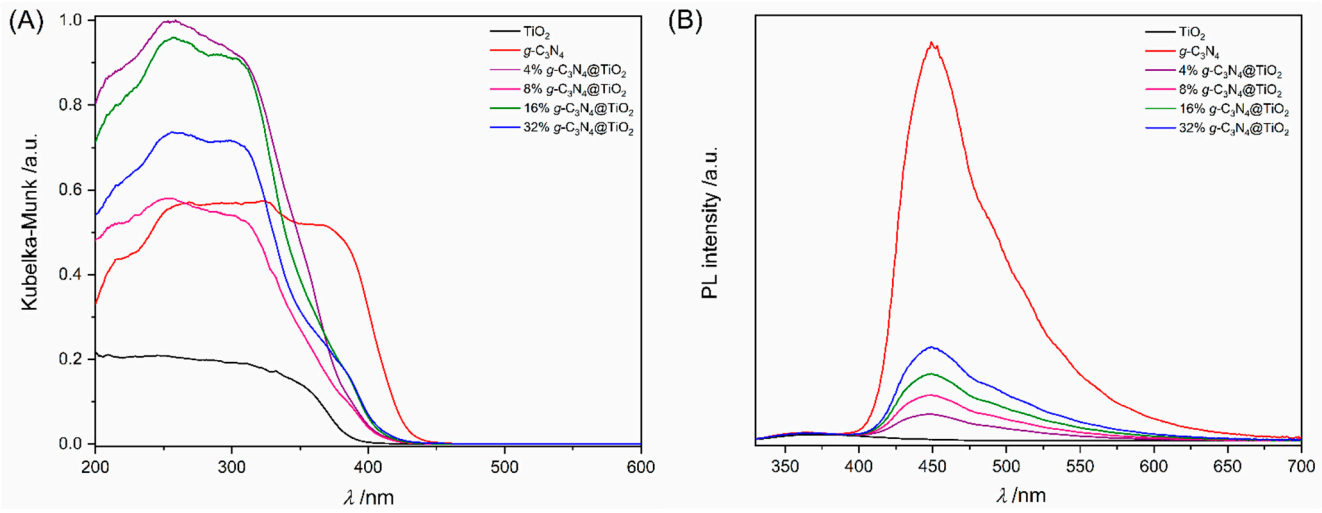

Figure 3. (**A**) The UV–Vis diffuse reflectance spectra and (**B**) room temperature photoluminescence (PL) spectra with 300 nm excitation for the synthesized g-C_3N_4, TiO_2, and their nanocomposites.

The optical properties of the studied materials were evaluated by UV–Vis diffuse reflectance in ultraviolet and visible regions, as shown in Figure 3A. Pure g-C_3N_4 absorbs much more in the visible region than pure TiO_2 nanoparticles, for which the Kubelka–Munk function is above zero only in the UV region. Thus, the absorption of the g-C_3N_4@TiO_2 nanocomposites broadens gradually towards longer wavelengths with the increasing content of g-C_3N_4. This points to a possible activity of these composites under solar light irradiation. The required band gap energy (Eg) was calculated by the Tauc method using

the Kubelka–Munk transformation with indirect band gap assumption [37]. The obtained values for pure *g*-C_3N_4 (2.85 eV) and pure TiO_2 (3.14 eV) agree well with values in the literature [38–40]. The wide Eg of pure TiO_2 nanoparticles was gradually narrowed with the increasing addition of the carbon nitride component into the composites [41]. The obtained Eg values are shown in Table 1.

Table 1. Band gap energies (Eg) of prepared materials.

Sample ID	Eg/eV
TiO_2	3.14
g-C_3N_4	2.85
4% *g*-C_3N_4@TiO_2	3.05
8% *g*-C_3N_4@TiO_2	2.99
16% *g*-C_3N_4@TiO_2	2.95
32% *g*-C_3N_4@TiO_2	2.94

The carbon nitride phase was much more evident in the photoluminescence (PL) of the composites (Figure 3B). Their emission spectra after 300 nm excitation resemble the characteristic emission of pure *g*-C_3N_4 at around the wavelength corresponding to the *g*-C_3N_4 band gap. It is a consequence of electron-hole recombination and several electron relaxations, which are not yet clearly understood. σ*-n transition usually emits at around 400 nm, but an absence of this peak has been regularly observed for *g*-C_3N_4 prepared under similar conditions as in this study. Some researchers attributed this to overlapping of π^* and σ* leading to absence of σ*-n and a π^*-n transition (with longer wavelength emission) instead [42–44]. Others keep attributing the first (and the highest) peak to the σ*-n transition, and explain its red shift with band gap narrowing due to processing at higher temperature (550 °C in the present case) [45–48]. Nevertheless, the two most intense peaks at around 450 nm and 480 nm are usually assigned to π^*-n and π^*-π transitions. Convolution of the obtained PL spectra from these two peaks already gives a good fit. However, an even better multipeak Gaussian fitting was obtained by assuming four overlapping peaks. This gave rise to two more peaks, one at 430 nm (probably related to σ*-n transition or π^* to some lower valence band state) and the lowest broad peak at around 510–520 nm, most probably related to transitions from defect states (e.g., C≡N triple bonds, NH_2 groups, vacancies, adatoms) and surface functional groups (e.g., –OH group and -NH_x dangling) to the valence band [48–50]. The obtained peak positions agree well with the values in previous PL experiments on *g*-C_3N_4 prepared at 550 °C for 2 h [29,42,46,51,52]. Below 400 nm, the composites, as well as pure TiO_2, exhibit a wide weak hump centred at around the wavelength corresponding to the TiO_2 indirect band gap (in accordance with previous measurements of similarly prepared TiO_2 nanoparticles [53]), which is related to various relaxations and recombination occurring in the TiO_2 component [54,55].

The specific surface area of pure TiO_2 nanoparticles, g-C_3N_4, and 32% *g*-C_3N_4@TiO_2 nanocomposite was found to be 114.3 m^2/g, 89.1 m^2/g, and 135.6 m^2/g, respectively, by the Brauner–Emmett–Teller (BET) method.

In Figure 4, the surface morphology of the pure TiO_2 nanoparticles, *g*-C_3N_4, and 32% *g*-C_3N_4@TiO_2 nanocomposite are presented. Figure 4A shows spherical-like nanoparticles of pure TiO_2 with sizes around 22.3±3.8 nm, which form agglomerates. Considering the SEM image of *g*-C_3N_4 (Figure 4B), irregular shapes were observed, varying in size up to 1.5±0.3µm. Finally, Figure 4C demonstrates good dispersal and embedment of TiO_2 particles on the surface of *g*-C_3N_4.

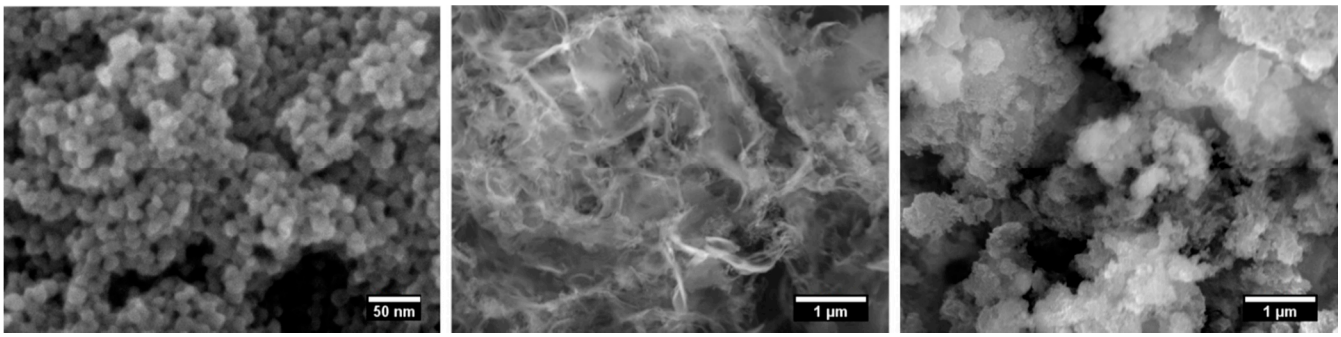

Figure 4. SEM images of prepared (**A**) pure TiO_2 nanoparticles, (**B**) *g*-C_3N_4, and (**C**) 32% *g*-C_3N_4@TiO_2 nanocomposite.

2.2. Evaluation of Photocatalytic Activity

Photocatalytic activity of the prepared samples was evaluated via MB degradation in ultrapure water under UV-A light irradiation. Figure 5A shows the MB adsorption and degradation rate in the presence of the photocatalysts. The adsorption–desorption equilibrium was investigated for 60 min in the dark. There was no adsorption of the dye onto the photocatalyst during this period (as evidenced by a static MB concentration in the "lamp off" region). In addition, a photolytic test in the absence of any catalysts was conducted to determine the stability of the dye and revealed that MB is stable under UV-A irradiation.

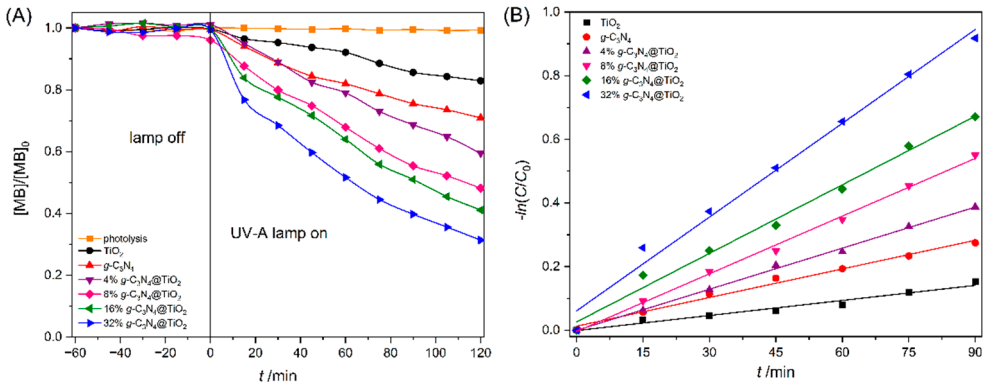

Figure 5. (**A**) Adsorption and photocatalytic activities of the prepared photocatalysts and (**B**) plotted first-order kinetics of MB degradation under UV-A irradiation (with wavelengths between 300 nm and 400 nm) with linear fits to obtain the rate constants.

MB concentration decreases with irradiation time in the presence of any of the investigated catalysts. The MB degradation efficiencies and rate constants after 90 min of irradiation are presented in Table 2 and the first-order kinetics of degradation is depicted in Figure 5B. These results show that all prepared *g*-C_3N_4@TiO_2 nanocomposites help degrade MB more efficiently than pure *g*-C_3N_4 or TiO_2 materials. The highest MB degradation rate was obtained with *g*-C_3N_4@TiO_2 containing 32 wt.% of *g*-C_3N_4.

MB degradation performances of TiO_2, *g*-C_3N_4, and *g*-C_3N_4@TiO_2 nanocomposites were also studied in a similar way under simulated solar irradiation for 90 min (Figure 6). The photolytic test revealed that MB is slowly photolyzed under simulated solar irradiation without any photocatalysts, while the photocatalytic reaction using the synthesized photocatalysts caused significant and notably faster MB degradation than the photolysis (Figure 6A). The photocatalytic activity of the synthesized *g*-C_3N_4@TiO_2 nanocomposites increases in correlation with the higher wt.% content of *g*-C_3N_4, as can be seen in Table 3. The rate of such degradation was also fitted to pseudo-first order kinetics. (Figure 6B) and deviates noticeably only in the composite with the highest *g*-C_3N_4 toTiO_2 ratio.

Table 2. The values of degradation efficiency of MB under UV-A irradiation and first-order rate constant (*k*).

Sample Name	Degradation Efficiency after 90 min/%	$k \times 10^{-3}$, min^{-1}
TiO_2	14	1.6
g-C_3N_4	24	3.0
4% *g*-C_3N_4@TiO_2	31	4.3
8% *g*-C_3N_4@TiO_2	45	6.0
16% *g*-C_3N_4@TiO_2	49	7.2
32% *g*-C_3N_4@TiO_2	60	9.8

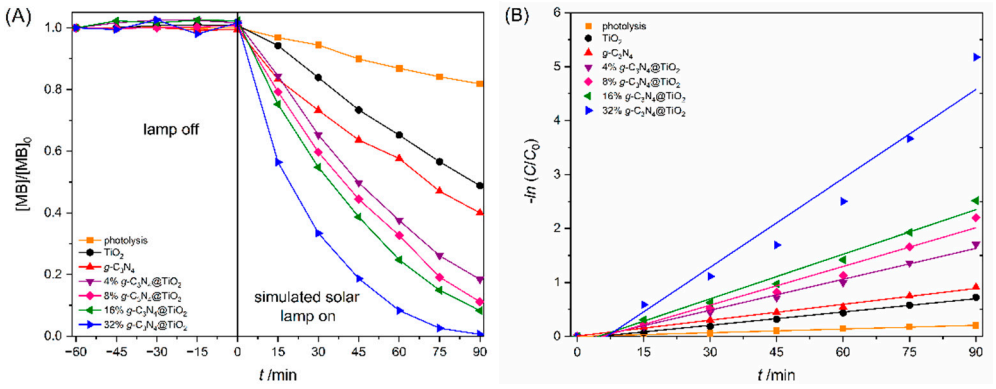

Figure 6. (**A**) Adsorption and photocatalytic activities of the prepared photocatalysts and (**B**) plotted first-order kinetics of MB degradation under simulated solar irradiation.

Table 3. The values of degradation efficiency of MB under simulated solar irradiation and first-order rate constant (*k*).

Sample Name	Degradation Efficiency after 90 min/%	$k \times 10^{-3}$, min^{-1}
photolysis	18	2.3
TiO_2	51	8.2
g-C_3N_4	60	9.8
4% *g*-C_3N_4@TiO_2	82	19.1
8% *g*-C_3N_4@TiO_2	89	23.9
16% *g*-C_3N_4@TiO_2	92	27.6
32% *g*-C_3N_4@TiO_2	99	54.9

The prepared nanocomposites displayed stronger photocatalytic activity than pure TiO_2 and *g*-C_3N_4 under UV-A, as well as simulated solar irradiation. In fact, the MB photodegradation efficiency was much higher under simulated solar irradiation than UV-A irradiation alone. This suggests that energies of the photons well below the band gap are also very important for photocatalysis, which is promising for utilization of this nanocomposites to degrade textile dyes under natural conditions.

Therefore, such applicability on the composite containing the highest fraction of *g*-C_3N_4 (32 wt.%) by irradiating the MB aqueous solution with natural sunlight was tested (Figure 7A). Photolysis without any catalyst was also examined as a reference, and it had already degraded 84% of MB within 60 min of irradiation. However, the photodegradation of MB with the chosen catalyst (32% *g*-C_3N_4@TiO_2) was much faster. After only 15 min of irradiation, 89% of MB vanished, and at the end of reaction (60 min), 99% was depleted. Moreover, this photodegradation under natural sunlight was even faster than in the simulated solar irradiated experiments, which is not surprising, since sunlight is a combination of high-energy ultraviolet, visible, and near-infrared light. On the other hand, the other two experimental light sources (UV-A and simulated solar) consisted of less powerful light emitters [56,57].

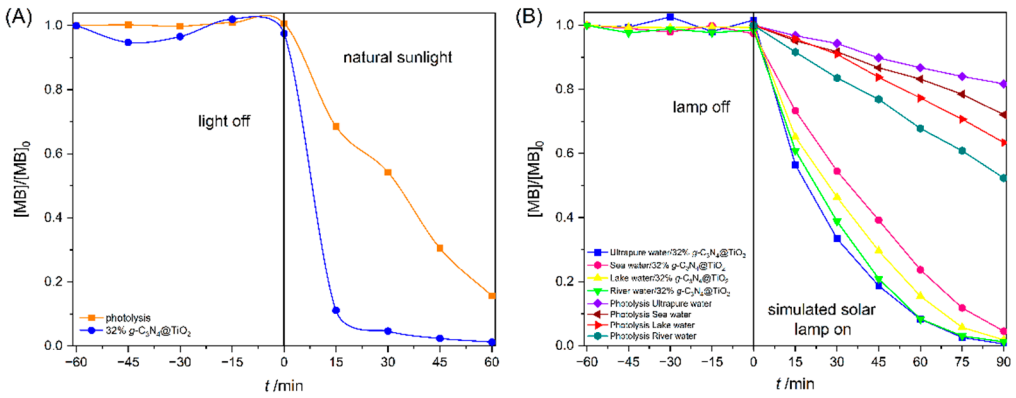

Figure 7. (**A**) Effect of natural sunlight irradiation on MB degradation and (**B**) Effect of different water bodies (ultrapure water, seawater, lake water, and river water) on the degradation efficiency of MB using 32% *g*-C_3N_4@TiO_2 under simulated solar irradiation.

Apart from the light source, photocatalysis also depends on the pH value and other properties of an aqueous environment [39,58]. To investigate this dependence, MB degradation was measured in ultrapure water, seawater, lake water, and river water during 90 min irradiation with simulated solar light and 32% *g*-C_3N_4@TiO_2 catalyst (Figure 7B). Adsorption of MB onto the catalyst's surface was negligible in all water bodies. However, when employing a simulated solar source of irradiation, MB degradation immediately began and continued almost to completion in all newly explored aqueous media within 90 min of simulated solar irradiation. The rate of first-order kinetics decreased in the order: ultrapure water > river water > lake water > seawater (Table 4).

Table 4. The values of pH and conductivity of water bodies, degradation efficiency of MB, and first-order rate constant (*k*) by using 32% *g*-C_3N_4@TiO_2 under simulated solar irradiation.

Water Bodies	pH	Conductivity /μS·cm^{-1}	Degradation Efficiency after 90 min/%	$k \times 10^{-3}$ /min^{-1}
Ultrapure water	6.20	0.378	99.4	54.9
Sea water	8.37	52,100	95.4	32.5
Lake water	7.95	351.2	98.1	42.7
River water	7.92	275.8	98.8	49.3

The photocatalytic degradation can be inhibited by some inorganic ions [59,60]. Additionally, various water matrices contain ions which can act as scavengers and influence the degradation rate of textile dyes. Conductivity measurements have been performed to determine the ionic concentration in different water matrices (Table 4). The lowest ion concentration has been noticed in ultra-pure water, while examples of river water, lake water and sea water demonstrated significant conductivity due to higher ion concentration [61]. The effective MB degradation in all investigated water matrices was determined, although the highest photodegradation rate was achieved in an ultra-pure water matrix as depicted in Figure 7B. Hence, the optimal concentration of ions in the water matrix is necessary to boost the photocatalytic decomposition of textile dyes, e.g., MB.

The obtained results suggest that 32% *g*-C_3N_4@TiO_2 can be effectively used in different water environments for sunlight degradation of organic pollutants. The observed minor differences in the photocatalytic activity of the same catalyst (32% *g*-C_3N_4@TiO_2) in different aqueous environments might be a consequence of their different pH or their organic or inorganic contents, such as certain ions acting as scavengers, which can slightly deactivate the catalyst or compete with the target MB dye for the active sites [56,59,62].

The reactive species help to convert the harmful organic pollutants (e.g., dyes) to simple and non-toxic molecules [63]. To determine the species involved in the photocatalytic process of MB photocatalytic degradation in ultrapure water, scavengers of $^{\bullet}OH$, h^+,

and e^- were added during the preparation of MB solution. Afterward, the simulated solar irradiation with 32% g-C_3N_4@TiO_2 catalyst was turned on. In Figure 8A, that MB degradation was decreased to 54.3%, 96.7%, and 66.2% after 90 min of irradiation in the presence of ethylenediaminetetraacetic acid (EDTA), isopropanol (IPA), and $AgNO_3$, respectively [64,65]. As can be seen in Figure 8A, the photocatalytic activity changed only slightly after the addition of IPA, which means that the $^{\bullet}OH$ radical plays a minor role in the photodegradation rate of MB. By contrast, when $AgNO_3$ and EDTA were added to the photocatalytic reaction, the photodegradation rate of MB decreased sharply, which indicates that e^- and h^+ play a significant role in the MB photodegradation process if 32% g-C_3N_4@TiO_2 catalyst is used under simulated solar irradiation. This is in good agreement with determined specific surface area of 32% g-C_3N_4@TiO_2. Furthermore, the contribution of h^+ seems to be the most important, followed by e^-, and the least contributing $^{\bullet}OH$.

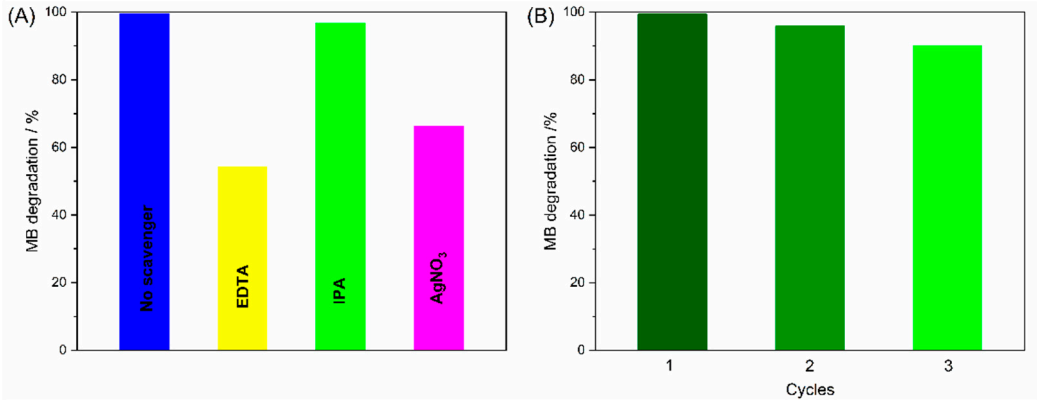

Figure 8. (**A**) Effect of different quenching ($^{\bullet}OH$, h^+, and e^-) on MB degradation in ultrapure water with scavenger dosage of 0.01 mol L^{-1} by using 32% *g*-C_3N_4@TiO_2 under simulated solar light after 90 min of irradiation and (**B**) reusability of prepared 32% *g*- C_3N_4@TiO_2 nanocomposite in three cycles.

Finally, a reusability test of 32% g-C_3N_4@TiO_2 nanocomposite for MB degradation was carried out for three consecutive cycles (Figure 8B). The MB degradation rate remained high (above 90%) in all three cycles, which confirmed good cycling stability of 32% g-C_3N_4@TiO_2 nanocomposite; 99.4%, 95.9% and 90.1% of MB were removed after the first, second and third cycles, respectively. The slight decline in the photodegradation rate could be associated with the mass loss of the catalyst after the successive cycle during the separation and washing process for recycling of the prepared 32% g-C_3N_4@TiO_2 nanocomposite [22,39].

The conducted scavenging experiments in the present study contributed to a better understanding of the enhanced photocatalytic efficiency of the *g*-C_3N_4@TiO_2 composite. In Figure 9, possible mechanisms of photocatalytic degradation induced by the *g*-C_3N_4@TiO_2 under solar radiation are schematically depicted. After exposing the photocatalyst to solar irradiation, the excited electrons (e^-) move from the conductive band (CB) of *g*-C_3N_4 to the CB of TiO_2. The transfer of electrons results in the formation of holes (h^+) in the valence band (VB) of *g*-C_3N_4 via a sensitization mechanism, which leads to the degradation of a pollutant. The CB of *g*-C_3N_4 has the role of electron donor to oxygen, leading to the formation of reactive $O_2^{\bullet-}$ species at TiO_2 surface, while holes at VB of TiO_2 cause the formation of hydroxyl radicals ($^{\bullet}OH$) at the *g*-C_3N_4 surface. Dye pollutant (MB), in turn, degrades into CO_2 and H_2O [66]. The photocatalytic decomposition of pollutants for the mechanism described above can be represented by the Equations (1)–(5):

$$g - C_3N_4@TiO_2 + h\nu \rightarrow g - C_3N_4@TiO_2\ (e^- + h^+) \quad (1)$$

$$e^- + O_2 \rightarrow O_2^{\bullet-} \quad (2)$$

$$h^+ + H_2O \rightarrow {}^{\bullet}OH \quad (3)$$

$$H_2O + O_2^{\bullet -} \rightarrow 2\,{}^{\bullet}OH \quad (4)$$

$$O_2^{\bullet -} / {}^{\bullet}OH / h^+ + \text{Pollutant} \rightarrow \text{Degradation products} \quad (5)$$

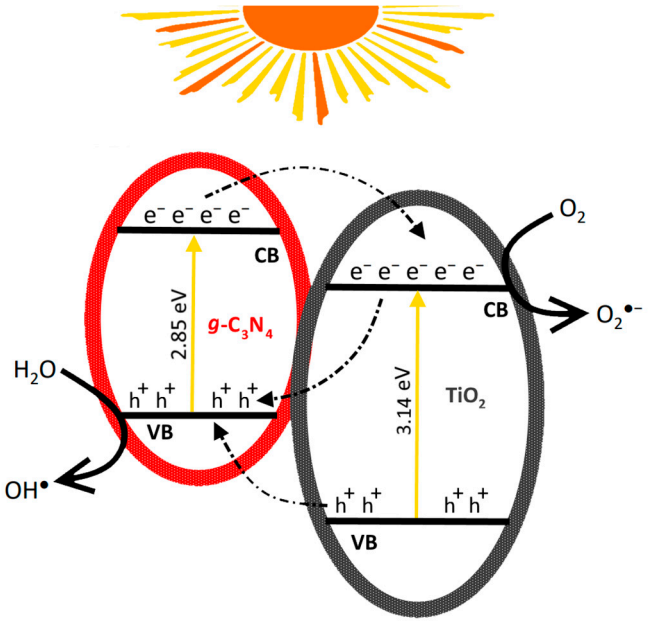

Figure 9. The proposed photocatalytic mechanisms of 32% *g*-C_3N_4@TiO_2 nanocomposite for MB degradation under simulated solar irradiation.

Furthermore, the formed holes transferred from VB of TiO_2 to VB of *g*-C_3N_4, and transfer of electrons vice versa, resulting in more effective suppression of the electron-hole recombination prior to the degradation reaction. In the end, a low probability of Z-scheme heterojunction occurrence exists due to the simplicity of the used preparation method. Z-scheme heterojunction recombination would increase the photocatalytic activity and would be more likely in materials with more interfaces. Nevertheless, the mentioned mechanism is described where its small amount of electrons could be transferring from the CB of TiO_2 to the VB of *g*-C_3N_4. Likewise, electrons could be transferred to the CB of *g*-C_3N_4, forming an electron storage reservoir resulting in the generation of holes in the VB of TiO_2. The latter prevents direct recombination of electrons leading to the most efficient degradation of pollutants observed so far [67].

3. Materials and Methods

3.1. Chemicals

Titanium (IV) isopropoxide ($Ti(C_3H_5O_{12})_4$, TTIP, 97%), urea (≥99%), ethylenediaminetetraacetic acid disodium salt dihydrate (EDTA-2Na), and silver nitrate ($AgNO_3$) were purchased from Merck KGaA (Darmstadt, Germany). 2-propanol (IPA, C_3H_7OH) and nitric acid (HNO_3, ≥65%) were purchased from Supelco (Darmstadt, Germany). Acetylacetone ($CH_3(CO)CH_2(CO)CH_3$) and methylene blue ($C_{16}H_{18}ClN_3S$, MB) were purchased from VWR Chemicals GmbH (Dresden, Germany). Ultra-pure water was used in all experiments within this work and produced in a LaboStar® PRO water purification system (resistivity 18.2 MΩ/cm at 24.5 °C, 0.2 µm sterile filter, Siemens, Germany).

3.2. Synthesis of TiO_2, g-C_3N_4, and g-C_3N_4@TiO_2 Nanocomposites

Bulk graphitic carbon nitride (*g*-C_3N_4) was prepared by a simple thermal procedure using urea as a precursor [39]. Briefly, 10 g of urea was put into a covered alumina ceramic crucible in a chamber furnace (Nabertherm, Germany), and was heated up to 550 °C at a rate of 5 °C/min and left for 2 h to dwell. Consequently, it was cooled naturally to room temperature. The obtained *g*-C_3N_4 powder was light yellow.

The pure TiO_2 nanoparticles were synthesized by a procedure previously reported [68]. A solution of TTIP was added drop by drop in IPA, under vigorous magnetic stirring. Acetylacetone was then added to the mixture, followed by 0.5 M of nitric acid. The TiO_2 colloidal solution was relocated into a Teflon-lined autoclave and kept in an oven at 180 °C for 6 h. Subsequently, the synthesized product was centrifuged at 5000 rpm to separate the precipitate from the supernatant, and then washed with ethanol and distilled water and dried.

The *g*-C_3N_4@TiO_2 nanocomposites were synthesized by adding the *g*-C_3N_4 powder during the sol-gel method of TiO_2 NPs preparation. Different amounts of prepared *g*-C_3N_4 nanosheets were dispersed into the TiO_2 colloidal solution, and the suspension further underwent an identical procedure as the pure TiO_2 colloidal solution. According to the used amount of *g*-C_3N_4 nanosheets, the nanocomposites are designated as Y *g*-C_3N_4@TiO_2, in which Y corresponds to the used amount of *g*-C_3N_4 nanosheets (4, 8, 16, and 32 wt.%). The synthesized pure TiO_2 and *g*-C_3N_4@TiO_2 nanocomposites were put into a ceramic crucible to anneal them at 300 °C with a heating rate of 3 °C/min for 2 h to dwell, and then cooled naturally to room temperature.

3.3. Physico-Chemical Characterization

The synthesized materials employed as photocatalysts were characterized by several characterization techniques. Fourier transform infrared spectroscopy-attenuated total reflectance (FTIR ATR) was characterized using a Shimadzu IR spectrometer (Kyoto, Japan) over a range of 400–4000 cm^{-1} at room temperature (resolution 4 cm^{-1}) to provide the information about functional groups. The crystalline phases were explored by an X-ray diffractometer (X'Pert PRO high-resolution X-ray diffractometer; PANalytical B.V., Almelo, Netherlands) using CuKα a radiation source (λ = 1.5406 Å) at 2θ ranging from 8° to 80° with step of 0.033°/100 s. A Shimadzu UV-Vis-NIR Spectrophotometer (UV-3600, Kyoto, Japan) with a reflectance sphere, using $BaSO_4$ as a reference, was used to measure the UV–Vis diffuse reflectance spectra (DRS). Photoluminescence spectra were recorded with an H1 Hybrid Multi-mode Microplate Reader (Synergy) on the powders in a UV-transparent 96-well plate with black walls (Greiner Bio-One UV-Star™ 96-well Microplates). Surface morphology was examined with a scanning electron microscope (SEM, Verios 4G HP, Thermo Fisher Scientific, Waltham, Massachusetts, USA). The specific surface area was performed by the BET method with a nitrogen adsorption analyzer (Quantachrome Nova 2000e, Anton Paar QuantaTec Inc., Graz, Austria).

3.4. Photolytic, Adsorption and Photocatalytic Measurements

The solution of MB (10 $mg{\cdot}L^{-1}$) was prepared by dissolving the weighed solid in ultrapure water. The photocatalytic tests of the as-prepared pure materials and nanocomposites were evaluated based on the photodegradation of MB under a UV-A lamp (Supratec 18W/73, Osram) and a simulated solar lamp (Osram Ultra Vitalux 300W). The radiation intensity of the UV-A lamp was 0.99 ± 0.3 mW/cm^2. Furthermore, the radiation intensity of the simulated solar lamp (64 mW/cm^2) has been previously reported [39]. Irradiation intensity was measured by a UV light meter (model YK-35UV). The different types of prepared photocatalysts were added into a quartz reactor in a concentration of 0.5 g L^{-1}. The reactor was then kept in a dark condition for 60 min, while stirring continuously (350 rpm) to ensure the photocatalyst surfaces achieved adsorption–desorption equilibrium. During the conducted tests, reaction aliquots at regular interval times were collected and centrifuged to remove the catalyst. To determine the concentration of the degraded MB, absorbance was monitored by UV–Vis spectroscopy on a Lambda 950 UV/VIS/NIR spectrophotometer (PerkinElmer, Waltham, MA, USA) in the 400–700 nm range using a quartz cuvette (Hellma Analytics, Stuttgart, Germany) with a path length of 10 mm. Photolytic tests were conducted without adding the catalysts under all used irradiations.

To simulate the natural conditions for possible water remediation, photodegradation of MB in different water environments, which were collected from river, lake, and sea, was

analysed. River water was collected near the source of the Sava River. Lake water was taken from Bled and seawater was collected on the coast near the city of Piran. Furthermore, the natural sunlight-driven photocatalysis was measured on 5 August 2022, at the Department for Nanostructured Materials, Jožef Stefan Institute in Ljubljana, Slovenia. The experiments with and without catalyst were carried out under natural sunlight (north 46° 2.517′, east 14° 29.241′, +360 m, WGS84) during sunny days with a high ultraviolet index (3.20–3.85 $mW \cdot cm^{-2}$).

To determine the degradation mechanism of MB, different scavengers were utilized: 10 mol L^{-1} of IPA, silver nitrate ($AgNO_3$), and EDTA-2Na were added to the MB solution to catch hydroxyl radical ($^{\bullet}OH$), electron (e^-), and hole (h^+), respectively.

To determine the reusable activity of the prepared photocatalyst, it was investigated by repeating three consecutive cycles under the same experimental conditions. After each cycle, the photocatalyst was collected through centrifugation, washed with absolute ethanol then with ultrapure water, and dried before reuse.

4. Conclusions

This work shows how the nature of prepared *g*-C_3N_4 and its amount affect the photocatalytic activity of *g*-C_3N_4@TiO_2 nanocomposite for MB degradation under different irradiation sources.

The bulk *g*-C_3N_4 was synthesized from low-cost precursor urea, and TiO_2 was synthesized via a two-step sol-gel and hydrothermal method. The synthesis of *g*-C_3N_4 and *g*-C_3N_4@TiO_2 via thermal polymerization and the hydrothermal synthesis approach is used for optimizing the synthesis parameters, such as mole ration of TiO_2 and *g*-C_3N_4, reaction temperature, and time, to facilitate upscaling of their fabrication. Hydrothermal synthesis for the preparation of *g*-C_3N_4@TiO_2 led to a simple experimental set-up and the effective fabrication of the nanocomposite. The physicochemical characterization of the prepared materials allowed the correlation of their structural, morphological, and optical attributes with the obtained photocatalytic results. The fabricated *g*-C_3N_4@TiO_2 demonstrated improved photodegradation of MB dye, as a model of organic pollutants, in the ultrapure water at natural pH = 6.20 under UV-A and simulated solar irradiation compared to pure TiO_2 and *g*-C_3N_4. The photodegradation efficiency of the prepared nanocomposites was found to be controlled by the amount (wt.%) of the *g*-C_3N_4, where 32 wt.% of *g*-C_3N_4 had the potential of removing 60% and 99% of MB dye after 90 min of under UV-A light and simulated solar irradiation. It was found that the amount of *g*-C_3N_4 plays an important role in the structural engineering of the prepared nanocomposite which reflects to photoactivity.

The advantages of high stability and easy recovery of the composites were demonstrated in the reusability evaluation. Thus, the obtained results of reusability (after three consecutive cycles) show no significant deactivation of the catalyst, which indicates a potential long-life span in the efficient photodegradation of pollutants. Thus, it can be concluded that prepared 32% g-C_3N_4@TiO_2 photocatalyst may be reused, which makes it a promising material for the removal of textile pollutants, especially MB. Furthermore, the high-efficiency removal of MB dye of the prepared *g*-C_3N_4@TiO_2 nanocomposite photocatalyst in diverse real water environments and under natural sunlight irradiation has also been confirmed, making it highly suitable for practical implementation.

Author Contributions: Conceptualization, M.K. (Martina Kocijan), M.V. and M.K. (Mario Kurtjak); methodology, M.K. (Martina Kocijan); software, M.K. (Martina Kocijan), M.V.; validation, M.K. (Martina Kocijan), M.V. and M.P.; formal analysis, M.K. (Martina Kocijan), M.V., M.K. (Mario Kurtjak), D.V. and M.P.; investigation, M.K. (Martina Kocijan) and M.V.; resources, M.P.; data curation, M.K. (Martina Kocijan), M.V. and M.P.; writing—original draft preparation, M.K. (Martina Kocijan), M.V., M.K. (Mario Kurtjak); writing—review and editing, L.Ć., M.K. (Mario Kurtjak), D.V. and M.P.; visualization, M.K. (Martina Kocijan), M.V., M.K. (Mario Kurtjak) and D.V.; supervision, L.Ć. and M.P.; project administration, M.P.; funding acquisition, M.P. All authors have read and agreed to the published version of the manuscript.

Funding: This research received no external funding.

Acknowledgments: The financial support of the Slovenian Research Agency is gratefully acknowledged (Project No. L2-1830, Program No. P2-0084, and Program No. P2-0091).

Conflicts of Interest: The authors declare no conflict of interest.

References

1. Khalid, S.; Shahid, M.; Natasha; Bibi, I.; Sarwar, T.; Shah, A.H.; Niazi, N.K. A Review of Environmental Contamination and Health Risk Assessment of Wastewater Use for Crop Irrigation with a Focus on Low and High-Income Countries. *Int. J. Environ. Res. Public Health* **2018**, *15*, 895. [CrossRef] [PubMed]
2. Zhou, H.; Smith, D.W. Advanced technologies in water and wastewater treatment. *Can. J. Civ. Eng.* **2001**, *28*, 49–66. [CrossRef]
3. Zhang, K.; Zhou, M.; Yang, K.; Yu, C.; Mu, P.; Yu, Z.; Lu, K.; Huang, W.; Dai, W. Photocatalytic H_2O_2 production and removal of Cr (VI) via a novel Lu_3NbO_7: Yb, Ho/CQDs/$AgInS_2$/In_2S_3 heterostructure with broad spectral response. *J. Hazard. Mater.* **2022**, *423*, 127172. [CrossRef] [PubMed]
4. Pandis, P.K.; Kalogirou, C.; Kanellou, E.; Vaitsis, C.; Savvidou, M.G.; Sourkouni, G.; Zorpas, A.A.; Argirusis, C. Key Points of Advanced Oxidation Processes (AOPs) for Wastewater, Organic Pollutants and Pharmaceutical Waste Treatment: A Mini Review. *ChemEngineering* **2022**, *6*, 8. [CrossRef]
5. Byrne, C.; Subramanian, G.; Pillai, S.C. Recent advances in photocatalysis for environmental applications. *J. Environ. Chem. Eng.* **2018**, *6*, 3531–3555. [CrossRef]
6. Liu, X.; Huang, W.Y.; Zhou, Q.; Chen, X.R.; Yang, K.; Li, D.; Dionysiou, D.D. Ag-decorated 3D flower-like Bi_2MoO_6/rGO with boosted photocatalytic performance for removal of organic pollutants. *Rare Met.* **2021**, *40*, 1086–1098. [CrossRef]
7. Yu, Z.; Yang, K.; Yu, C.; Lu, K.; Huang, W.; Xu, L.; Zou, L.; Wang, S.; Chen, Z.; Hu, J.; et al. Steering Unit Cell Dipole and Internal Electric Field by Highly Dispersed Er atoms Embedded into NiO for Efficient CO_2 Photoreduction. *Adv. Funct. Mater.* **2022**, *32*, 2111999. [CrossRef]
8. Darkwah, W.K.; Ao, Y. Mini Review on the Structure and Properties (Photocatalysis), and Preparation Techniques of Graphitic Carbon Nitride Nano-Based Particle, and Its Applications. *Nanoscale Res. Lett.* **2018**, *13*, 388. [CrossRef]
9. Ibhadon, A.O.; Fitzpatrick, P. Heterogeneous Photocatalysis: Recent Advances and Applications. *Catalysts* **2013**, *3*, 189–218. [CrossRef]
10. Fagan, R.; McCormack, D.E.; Dionysiou, D.D.; Pillai, S.C. A review of solar and visible light active TiO_2 photocatalysis for treating bacteria, cyanotoxins and contaminants of emerging concern. *Mater. Sci. Semicond. Process.* **2016**, *42*, 2–14. [CrossRef]
11. Zhang, Y.; Zhang, N.; Tang, Z.-R.; Xu, Y.-J. Improving the photocatalytic performance of graphene–TiO_2 nanocomposites via a combined strategy of decreasing defects of graphene and increasing interfacial contact. *Phys. Chem. Chem. Phys.* **2012**, *14*, 9167–9175. [CrossRef] [PubMed]
12. Fu, M.; Liao, J.; Dong, F.; Li, H.; Liu, H. Growth of g-C_3N_4 Layer on Commercial TiO_2 for Enhanced Visible Light Photocatalytic Activity. *J. Nanomater.* **2014**, *2014*, 869094. [CrossRef]
13. Mohini, R.; Lakshminarasimhan, N. Coupled semiconductor nanocomposite *g*-C_3N_4/TiO_2 with enhanced visible light photocatalytic activity. *Mater. Res. Bull.* **2016**, *76*, 370–375. [CrossRef]
14. Li, C.; Zhu, D.; Cheng, S.; Zuo, Y.; Wang, Y.; Ma, C.; Dong, H. Recent research progress of bimetallic phosphides-based nanomaterials as cocatalyst for photocatalytic hydrogen evolution. *Chin. Chem. Lett.* **2022**, *33*, 1141–1153. [CrossRef]
15. Miranda, C.; Mansilla, H.; Yáñez, J.; Obregón, S.; Colón, G. Improved photocatalytic activity of *g*-C_3N_4/TiO_2 composites prepared by a simple impregnation method. *J. Photochem. Photobiol. A Chem.* **2013**, *253*, 16–21. [CrossRef]
16. Boonprakob, N.; Wetchakun, N.; Phanichphant, S.; Waxler, D.; Sherrell, P.; Nattestad, A.; Chen, J.; Inceesungvorn, B. Enhanced visible-light photocatalytic activity of *g*-C_3N_4/TiO_2 films. *J. Colloid Interface Sci.* **2014**, *417*, 402–409. [CrossRef]
17. Yu, T.; Liu, L.; Yang, F. Heterojunction between anodic TiO_2/*g*-C_3N_4 and cathodic WO_3/W nano-catalysts for coupled pollutant removal in a self-biased system. *Chinese J. Catal.* **2017**, *38*, 270–277. [CrossRef]
18. Tian, Q.; Shen, X.; Wang, Z.; Zhu, B.; Osotsi, M.I.; Xie, X.; Jin, Y.; Chen, Z.; Zhang, L. Growth of Cu_2O Spherical Superstructures on *g*-C_3N_4 as Efficient Visible-Light-Driven p-n Heterojunction Photocatalysts for Degrading Various Organic Pollutants. *J. Nanosci. Nanotechnol.* **2018**, *18*, 7355–7363. [CrossRef]
19. Liu, H.; Zhang, Z.-G.; He, H.-W.; Wang, X.-X.; Zhang, J.; Zhang, Q.-Q.; Tong, Y.-F.; Liu, H.-L.; Ramakrishna, S.; Yan, S.-Y.; et al. One-Step Synthesis Heterostructured *g*-C_3N_4/TiO_2 Composite for Rapid Degradation of Pollutants in Utilizing Visible Light. *Nanomaterials* **2018**, *8*, 842. [CrossRef]
20. Xia, Y.; Xu, L.; Peng, J.; Han, J.; Guo, S.; Zhang, L.; Han, Z.; Komarneni, S. TiO_2@*g*-C_3N_4 core/shell spheres with uniform mesoporous structures for high performance visible-light photocatalytic application. *Ceram. Int.* **2019**, *45*, 18844–18851. [CrossRef]
21. Tang, Q.; Meng, X.; Wang, Z.; Zhou, J.; Tang, H. One-step electrospinning synthesis of TiO_2/*g*-C_3N_4 nanofibers with enhanced photocatalytic properties. *Appl. Surf. Sci.* **2018**, *430*, 253–262. [CrossRef]
22. Razali, M.H.; Md Fauzi, M.A.F.; Mohd Azam, B.; Yusoff, M. *g*-C_3N_4/TiO_2 nanocomposite photocatalyst for methylene blue photodegradation under visible light. *Appl. Nanosci.* **2022**, *12*, 3197–3206. [CrossRef]
23. Song, G.; Chu, Z.; Jin, W.; Sun, H. Enhanced performance of *g*-C_3N_4/TiO_2 photocatalysts for degradation of organic pollutants under visible light. *Chinese J. Chem. Eng.* **2015**, *23*, 1326–1334. [CrossRef]

24. Ma, L.; Wang, G.; Jiang, C.; Bao, H.; Xu, Q. Synthesis of core-shell TiO_2@*g*-C_3N_4 hollow microspheres for efficient photocatalytic degradation of rhodamine B under visible light. *Appl. Surf. Sci.* **2018**, *430*, 263–272. [CrossRef]
25. Li, K.; Gao, S.; Wang, Q.; Xu, H.; Wang, Z.; Huang, B.; Dai, Y.; Lu, J. In-Situ-Reduced Synthesis of Ti^{3+} Self-Doped TiO_2/*g*-C_3N_4 Heterojunctions with High Photocatalytic Performance under LED Light Irradiation. *ACS Appl. Mater. Interfaces* **2015**, *7*, 9023–9030. [CrossRef]
26. Barzegar, M.H.; Sabzehmeidani, M.M.; Ghaedi, M.; Avargani, V.M.; Moradi, Z.; Roy, V.A.L.; Heidari, H. S-scheme heterojunction *g*-C_3N_4/TiO_2 with enhanced photocatalytic activity for degradation of a binary mixture of cationic dyes using solar parabolic trough reactor. *Chem. Eng. Res. Des.* **2021**, *174*, 307–318. [CrossRef]
27. Adeleye, A.T.; John, K.I.; Adeleye, P.G.; Akande, A.A.; Banjoko, O.O. One-dimensional titanate nanotube materials: Heterogeneous solid catalysts for sustainable synthesis of biofuel precursors/value-added chemicals—A review. *J. Mater. Sci.* **2021**, *56*, 18391–18416. [CrossRef]
28. Dong, G.; Zhao, K.; Zhang, L. Carbon self-doping induced high electronic conductivity and photoreactivity of *g*-C_3N_4. *Chem. Commun.* **2012**, *48*, 6178–6180. [CrossRef]
29. Zhu, B.; Xia, P.; Li, Y.; Ho, W.; Yu, J. Fabrication and photocatalytic activity enhanced mechanism of direct Z-scheme *g*-C_3N_4/Ag_2WO_4 photocatalyst. *Appl. Surf. Sci.* **2017**, *391*, 175–183. [CrossRef]
30. Thomas, A.; Fischer, A.; Goettmann, F.; Antonietti, M.; Müller, J.O.; Schlögl, R.; Carlsson, J.M. Graphitic carbon nitride materials: Variation of structure and morphology and their use as metal-free catalysts. *J. Mater. Chem.* **2008**, *18*, 4893–4908. [CrossRef]
31. Aleksandrzak, M.; Baranowska, D.; Kukulka, W.; Onyszko, M.; Zielinska, B.; Mijowska, E. Bifunctional polymeric carbon nitride via tuning fabrication conditions for photocatalysis. *Catalysts* **2021**, *11*, 651. [CrossRef]
32. Zhang, H.; Wang, X.; Li, N.; Xia, J.; Meng, Q.; Ding, J.; Lu, J. Synthesis and characterization of TiO_2/graphene oxide nanocomposites for photoreduction of heavy metal ions in reverse osmosis concentrate. *RSC Adv.* **2018**, *8*, 34241–34251. [CrossRef] [PubMed]
33. Chen, Y.F.; Lee, C.Y.; Yeng, M.Y.; Chiu, H.T. The effect of calcination temperature on the crystallinity of TiO_2 nanopowders. *J. Cryst. Growth* **2003**, *247*, 363–370. [CrossRef]
34. Amorin, L.H.; Suzuki, V.Y.; De Paula, N.H.; Duarte, J.L.; Da Silva, M.A.T.; Taft, C.A.; De Almeida La Porta, F. Electronic, structural, optical, and photocatalytic properties of graphitic carbon nitride. *New J. Chem.* **2019**, *43*, 13647–13653. [CrossRef]
35. Li, J.; Liu, Y.; Li, H.; Chen, C. Fabrication of *g*-C_3N_4/TiO_2 composite photocatalyst with extended absorption wavelength range and enhanced photocatalytic performance. *J. Photochem. Photobiol. A Chem.* **2016**, *317*, 151–160. [CrossRef]
36. Jiang, Z.; Zhu, C.; Wan, W.; Qian, K.; Xie, J. Constructing graphite-like carbon nitride modified hierarchical yolk-shell TiO_2 spheres for water pollution treatment and hydrogen production. *J. Mater. Chem. A* **2016**, *4*, 1806–1818. [CrossRef]
37. Makuła, P.; Pacia, M.; Macyk, W. How To Correctly Determine the Band Gap Energy of Modified Semiconductor Photocatalysts Based on UV-Vis Spectra. *J. Phys. Chem. Lett.* **2018**, *9*, 6814–6817. [CrossRef]
38. Pham, M.T.; Luu, H.Q.; Nguyen, T.M.T.; Tran, H.H.; You, S.J.; Wang, Y.F. Rapid and Scalable Fabrication of TiO_2@*g*-C_3N_4 Heterojunction for Highly Efficient Photocatalytic NO Removal under Visible Light. *Aerosol Air Qual. Res.* **2021**, *21*, 210276. [CrossRef]
39. Kocijan, M.; Ćurković, L.; Radošević, T.; Podlogar, M. Enhanced Photocatalytic Activity of Hybrid rGO@TiO_2/CN Nanocomposite for Organic Pollutant Degradation under Solar Light Irradiation. *Catalysts* **2021**, *11*, 1023. [CrossRef]
40. Alfaifi, M.Q.; Bagabas, A.A. Preparation, characterization, and application in water purification of *g*-C_3N_4/I-TiO_2 composite photocatalysts. *Adv. Mater. Sci.* **2019**, *4*, 1–10. [CrossRef]
41. Parvathiraja, C.; Katheria, S.; Siddiqui, M.R.R.; Wabaidur, S.M.M.; Islam, M.A.A.; Lai, W.-C. Activated Carbon-Loaded Titanium Dioxide Nanoparticles and Their Photocatalytic and Antibacterial Investigations. *Catalysts* **2022**, *12*, 834. [CrossRef]
42. Zhang, Y.; Pan, Q.; Chai, G.; Liang, M.; Dong, G.; Zhang, Q.; Qiu, J. Synthesis and luminescence mechanism of multicolor-emitting *g*-C_3N_4 nanopowders by low temperature thermal condensation of melamine. *Sci. Rep.* **2013**, *3*, 1943. [CrossRef]
43. Bian, J.; Li, J.; Kalytchuk, S.; Wang, Y.; Li, Q.; Lau, T.C.; Niehaus, T.A.; Rogach, A.L.; Zhang, R.Q. Efficient emission facilitated by multiple energy level transitions in uniform graphitic carbon nitride films deposited by thermal vapor condensation. *ChemPhysChem* **2015**, *16*, 954–959. [CrossRef]
44. Bayan, S.; Midya, A.; Gogurla, N.; Singha, A.; Ray, S.K. Origin of Modified Luminescence Response in Reduced Graphitic Carbon Nitride Nanosheets. *J. Phys. Chem. C* **2017**, *121*, 19383–19391. [CrossRef]
45. Yuan, Y.; Zhang, L.; Xing, J.; Utama, M.I.B.; Lu, X.; Du, K.; Li, Y.; Hu, X.; Wang, S.; Genç, A.; et al. High-yield synthesis and optical properties of *g*-C_3N_4. *Nanoscale* **2015**, *7*, 12343–12350. [CrossRef] [PubMed]
46. Das, D.; Shinde, S.L.; Nanda, K.K. Temperature-Dependent Photoluminescence of *g*-C_3N_4: Implication for Temperature Sensing. *ACS Appl. Mater. Interfaces* **2016**, *8*, 2181–2186. [CrossRef] [PubMed]
47. Chubenko, E.B.; Baglov, A.V.; Leonenya, M.S.; Yablonskii, G.P.; Borisenko, V.E. Structure of Photoluminescence Spectra of Oxygen-Doped Graphitic Carbon Nitride. *J. Appl. Spectrosc.* **2020**, *87*, 9–14. [CrossRef]
48. Zhang, X.; Jiang, S.P.; Yang, P. Bright and tunable photoluminescence from the assembly of red *g*-C_3N_4 nanosheets. *J. Lumin.* **2021**, *235*, 118055. [CrossRef]
49. Choudhury, B.; Paul, K.K.; Sanyal, D.; Hazarika, A.; Giri, P.K. Evolution of Nitrogen-Related Defects in Graphitic Carbon Nitride Nanosheets Probed by Positron Annihilation and Photoluminescence Spectroscopy. *J. Phys. Chem. C* **2018**, *122*, 9209–9219. [CrossRef]

50. Tang, W.; Tian, Y.; Chen, B.; Xu, Y.; Li, B.; Jing, X.; Zhang, J.; Xu, S. Supramolecular Copolymerization Strategy for Realizing the Broadband White Light Luminescence Based on N-Deficient Porous Graphitic Carbon Nitride (g-C_3N_4). *ACS Appl. Mater. Interfaces* **2020**, *12*, 6396–6406. [CrossRef]
51. Samanta, S.; Martha, S.; Parida, K. Facile synthesis of Au/g-C_3N_4 nanocomposites: An inorganic/organic hybrid plasmonic photocatalyst with enhanced hydrogen gas evolution under visible-light irradiation. *ChemCatChem* **2014**, *6*, 1453–1462. [CrossRef]
52. Hu, S.W.; Yang, L.W.; Tian, Y.; Wei, X.L.; Ding, J.W.; Zhong, J.X.; Chu, P.K. Non-covalent doping of graphitic carbon nitride with ultrathin graphene oxide and molybdenum disulfide nanosheets: An effective binary heterojunction photocatalyst under visible light irradiation. *J. Colloid Interface Sci.* **2014**, *431*, 42–49. [CrossRef]
53. Horti, N.C.; Kamatagi, M.D.; Patil, N.R.; Nataraj, S.K.; Sannaikar, M.S.; Inamdar, S.R. Synthesis and photoluminescence properties of titanium oxide (TiO_2) nanoparticles: Effect of calcination temperature. *Optik* **2019**, *194*, 163070. [CrossRef]
54. Abazović, N.D.; Čomor, M.I.; Dramićanin, M.D.; Jovanović, D.J.; Ahrenkiel, S.P.; Nedeljković, J.M. Photoluminescence of anatase and rutile TiO_2 particles. *J. Phys. Chem. B* **2006**, *110*, 25366–25370. [CrossRef]
55. Pallotti, D.K.; Passoni, L.; Maddalena, P.; Di Fonzo, F.; Lettieri, S. Photoluminescence Mechanisms in Anatase and Rutile TiO_2. *J. Phys. Chem. C* **2017**, *121*, 9011–9021. [CrossRef]
56. Jiménez-Salcedo, M.; Monge, M.; Tena, M.T. The photocatalytic degradation of sodium diclofenac in different water matrices using g-C_3N_4 nanosheets: A study of the intermediate by-products and mechanism. *J. Environ. Chem. Eng.* **2021**, *9*, 105827. [CrossRef]
57. Iovino, P.; Chianese, S.; Canzano, S.; Prisciandaro, M.; Musmarra, D. Ibuprofen photodegradation in aqueous solutions. *Environ. Sci. Pollut. Res.* **2016**, *23*, 22993–23004. [CrossRef]
58. Shehzad, N.; Tahir, M.; Johari, K.; Murugesan, T.; Hussain, M. A critical review on TiO_2 based photocatalytic CO_2 reduction system: Strategies to improve efficiency. *J. CO_2 Util.* **2018**, *26*, 98–122. [CrossRef]
59. Hu, L.; Flanders, P.M.; Miller, P.L.; Strathmann, T.J. Oxidation of sulfamethoxazole and related antimicrobial agents by TiO_2 photocatalysis. *Water Res.* **2007**, *41*, 2612–2626. [CrossRef]
60. Petala, A.; Mantzavinos, D.; Frontistis, Z. Impact of water matrix on the photocatalytic removal of pharmaceuticals by visible light active materials. *Curr. Opin. Green Sustain. Chem.* **2021**, *28*, 100445. [CrossRef]
61. Dharwadkar, S.; Yu, L.; Achari, G. Photocatalytic degradation of sulfolane using a led-based photocatalytic treatment system. *Catalysts* **2021**, *11*, 624. [CrossRef]
62. Cruz, M.; Gomez, C.; Duran-Valle, C.J.; Pastrana-Martínez, L.M.; Faria, J.L.; Silva, A.M.T.; Faraldos, M.; Bahamonde, A. Bare TiO_2 and graphene oxide TiO_2 photocatalysts on the degradation of selected pesticides and influence of the water matrix. *Appl. Surf. Sci.* **2017**, *416*, 1013–1021. [CrossRef]
63. Faisal, M.; Alsaiari, M.; Rashed, M.A.; Harraz, F.A. Biomass-derived active Carbon@ZnO/SnO_2 novel visible-light photocatalyst for rapid degradation of linezolid antibiotic and imidacloprid insecticide. *J. Taiwan Inst. Chem. Eng.* **2021**, *120*, 313–324. [CrossRef]
64. Vavilapalli, D.S.; Peri, R.G.; Sharma, R.K.; Goutam, U.K.; Muthuraaman, B.; Ramachandra Rao, M.S.; Singh, S. g-C_3N_4/$Ca_2Fe_2O_5$ heterostructures for enhanced photocatalytic degradation of organic effluents under sunlight. *Sci. Rep.* **2021**, *11*, 19639. [CrossRef]
65. Gogoi, D.; Makkar, P.; Ghosh, N.N. Solar Light-Irradiated Photocatalytic Degradation of Model Dyes and Industrial Dyes by a Magnetic $CoFe_2O_4$-gC_3N_4 S-Scheme Heterojunction Photocatalyst. *ACS Omega* **2021**, *6*, 4831–4841. [CrossRef]
66. Md Fauzi, M.A.F.; Razali, M.H.; Osman, M.U.; Mohd Azam, B. Synthesis and characterisation of TiO_2/g-C_3N_4 as photocatalyst for photodegradation of dyes, phenol and caffeine. *Adv. Mater. Process. Technol.* **2022**, 1–21. [CrossRef]
67. Islam, M.R.; Chakraborty, A.K.; Gafur, M.A.; Rahman, M.A.; Rahman, M.H. Easy preparation of recyclable thermally stable visible-light-active graphitic-C_3N_4/TiO_2 nanocomposite photocatalyst for efficient decomposition of hazardous organic industrial pollutants in aqueous medium. *Res. Chem. Intermed.* **2019**, *45*, 1753–1773. [CrossRef]
68. Kocijan, M.; Ćurković, L.; Ljubas, D.; Mužina, K.; Bačić, I.; Radošević, T.; Podlogar, M.; Bdikin, I.; Otero-Irurueta, G.; Hortigüela, M.J.; et al. Graphene-Based TiO_2 Nanocomposite for Photocatalytic Degradation of Dyes in Aqueous Solution under Solar-Like Radiation. *Appl. Sci.* **2021**, *11*, 3966. [CrossRef]